Room Temperature Weak-to-Strong Coupling and the Emergence of Collective Emission from Quantum Dots Coupled to Plasmonic Arrays

Ravindra Kumar Yadav,[†] Marc R. Bourgeois,[‡] Charles Cherqui,[‡] Xitlali G. Juarez,[¶] Weijia Wang,[§] Teri W. Odom,^{*,§} George C. Schatz,^{*,‡} and Jaydeep Kumar Basu^{*,†}

†Department of Physics, Indian Institute of Science, Bangalore 560 012, India.

‡Department of Chemistry, Northwestern University, Evanston, Illinois 60208, USA.

¶Department of Materials Science and Engineering, Northwestern University, Evanston, Illinois 60208, USA.

§Graduate Program in Applied Physics, Northwestern University, Evanston, Illinois 60208, USA.

E-mail: todom@northwestern.edu; g-schatz@northwestern.edu; basu@iisc.ac.in

Abstract

Colloidal quantum dot (CQD) assemblies exhibit interesting opto-electronic properties when coupled to optical resonators ranging from Purcell enhanced emission to the emergence of hybrid electronic and photonic polariton states in the weak and strong coupling limits, respectively. Here, experiments exploring the weak-to-strong coupling transition in CQD-plasmonic lattice hybrid devices at room temperature are presented for varying CQD concentrations. To interpret these results, generalized retarded Fano-Anderson and effective medium models are developed. Individual CQDs are found to interact locally with the lattice yielding Purcell-enhanced emission. At high

CQD densities, polariton states emerge as two-peak structures in the photoluminescence, with a third polariton peak, due to collective CQD emission, appearing at still higher CQD concentrations. Our results demonstrate that CQD-lattice plasmon devices represent a highly-flexible platform for the manipulation of collective spontaneous emission using lattice plasmons, which could find applications in opto-electronics, ultrafast optical switches, and quantum information science.

Keywords

quantum dot, surface lattice resonances, lattice plasmons, strong coupling, Purcell factor, polariton.

Controlling the electromagnetic interactions between quantum emitters and localized surface plasmons (LSPs), the collective excitations of conduction band electrons in metal nanoparticles (NPs), in the weak, intermediate, and strong coupling regimes has been the focus of an intense research effort in recent years. 1-4 Interest in this topic is motivated by the ability of LSPs to confine light to sub-diffraction-limited mode volumes, which can drive coherence effects in collective quantum emitter systems, leading to applications in coherent light generation, photochemistry, quantum information processing, and quantum photonic fluids. 5-10 The weak and intermediate coupling regimes are associated with enhancement of the emission and absorption rates of nearby resonant emitters, while the strong coupling regime allows for coherent energy transfer between emitters and LSPs. The resulting hybridized polariton states are separated by the Rabi splitting energy $\hbar\Omega_R$. 11,12 One drawback to using LSPs to mediate emitter-emitter interactions is their intrinsic Ohmic and radiative losses, which must be mitigated to reach the strong coupling regime. 1,13,14 Periodic arrays of NPs, on the other hand, support hybrid photonic-LSP modes known as plasmonic surface lattice resonances (SLRs) that exhibit lifetimes several orders of magnitude higher than single particle LSPs without sacrificing the field enhancement properties that make LSPs attractive. 15-17 The periodicity of the NP lattice gives rise to SLR dispersion energies $E(\mathbf{k}_{\parallel})$ that are periodic in k-space. ¹⁸ Bragg scattering at high-symmetry points of the Brillouin zone leads to the formation of band-edge states characterized by a large photonic density of states that may be exploited to mediate SLR-QE interactions.

In the weak coupling regime, the optical properties of plasmonic SLRs have been leveraged to enhance single photon emission from quantum emitters (QEs) *via* the Purcell effect, and room-temperature lasing from solutions of organic dye molecules coupled to Γ point ($|\mathbf{k}_{\parallel}| = 0$) SLRs. ^{19–24} More recently, lasing from dye molecules coupled to the Γ and K point SLRs supported by non-Bravais plasmonic honeycomb lattices was also demonstrated. ^{25,26} Room-temperature plasmon-exciton polariton lasing and Bose-Einstein condensation of SLRs into a single quantum state has also been observed in strongly coupled SLR-organic dye systems. ^{27–29} Colloidal quantum dots (CQDs) are an especially attractive class of QEs owing to high quantum efficiencies and broadband spectral tunability, ^{30–32} which has made them critical components in a variety of photonic devices, ³³ including nanolasers, ^{34,35} photovoltaics, ^{36,37} and photodetectors. ³⁸ Despite the achievement of strong coupling between SLRs and organic molecules, ^{39–41} carbon nanotubes, ⁴² and TMDCs, ⁴³ and of weak coupling between SLRs and CQDs, ⁴⁴ strong coupling between SLRs and CQD assemblies has not yet been reported. The barrier to progress, in this case, is related to the experimental challenges involved in fabricating CQD layers of a high enough concentration while also maintaining a sufficiently narrow CQD size distribution.

In this paper, we explore the tunable coupling between exciton-supporting CQDs and SLRs in Ag NP arrays through QE density variation and SLR-CQD resonance detuning. Through photo-luminescence (PL) measurements and theory development for the hybridized SLR-CQD system, we demonstrate that as the CQD density is increased, the system transitions between the weak, intermediate, and strong coupling regimes. Further, we show that when CQD densities are near saturation levels, a third hybridized mode appears in the PL spectrum that electromagnetic calculations indicate arises from a polariton state accessible at high emitter densities. Our results extend the study of strong coupling between plasmonic SLRs and QEs to a separate class of CQD emitters and highlights the density-dependent transition from localized to delocalized coupling.

Results and Discussion

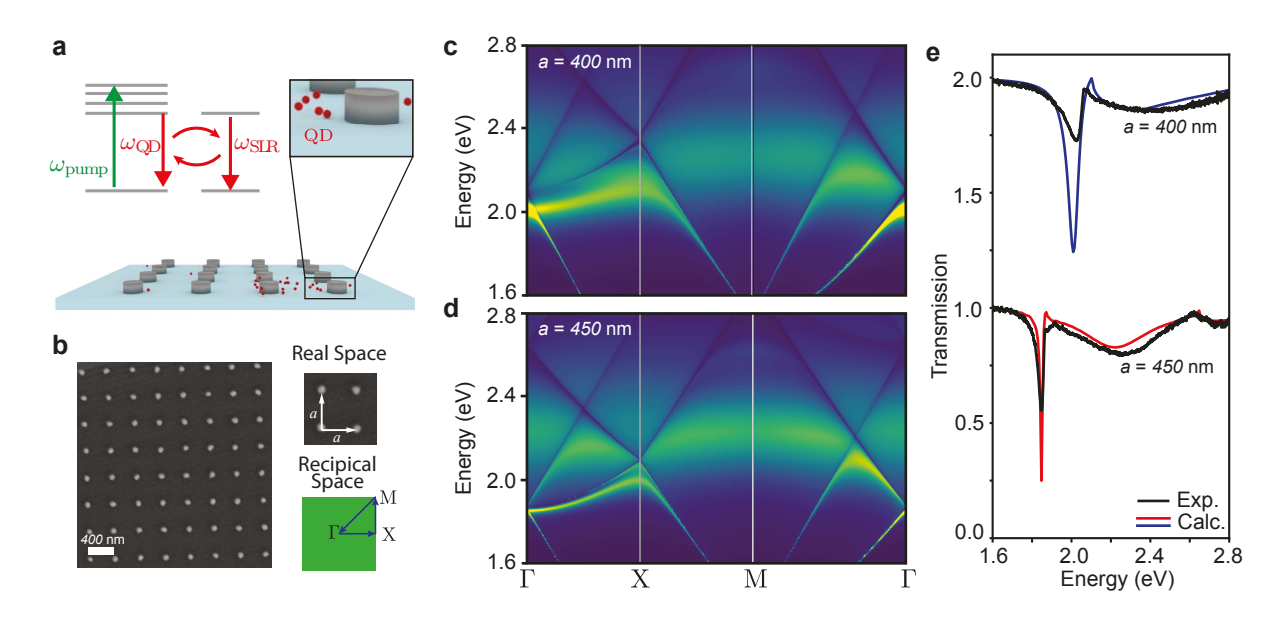


Figure 1: Experimental setup and plasmonic lattice characterization (a) Schematic of CDQ-plasmonic lattice system. (b) SEM image of fabricated NP array with a=400 nm periodicity. The scale bar is 400 nm. The diameter and height of the Ag NPs were 80 nm and 40 nm, respectively. The green square represents the Brillouin zone with the irreducible portion connecting the Γ , X, and M points outlined in blue. (c) Dispersion diagram of plasmonic SLR modes of the a=400 nm array along the boundary of the irreducible Brillouin zone calculated using the coupled dipole method. (d) Same as (c), but for the a=450 nm array. (e) Comparison of measured (black) and FDTD (blue and red) Γ point transmission spectra for a=400 nm and a=450 nm arrays.

Figure 1(a) shows a schematic of the measured SLR-CQD system. Synthesized CdSe/ZnS CQDs (Methods section) were excited either directly on glass substrates or within NP arrays (also supported on glass) with 2.4 eV light through an objective lens in an inverted fluorescence microscope. PL from the CQD band-edge state was emitted near 2.0 eV and collected through the same objective lens. Two square lattices of Ag NPs with 80 nm diameter and 40 nm height were fabricated with lattice constants a = 400 nm, and a = 450 nm (SEM images in Figure 1(b)), placing the Γ point SLR modes at approximately 2 eV and 1.8 eV, respectively, for a background index of refraction n = 1.47. Extinction efficiency spectra (Methods section) were calculated for \mathbf{k}_{\parallel} along the boundary of the irreducible Brillouin zone of each lattice using the coupled dipole method (Figure 1(c-d)). The extinction is maximized near the Γ and X points due to the large density of photonic states available at the band-edge states created at high-symmetry points of the Brillouin zone. The

measured Γ point transmission spectra of the two NP arrays were in close agreement with transmission spectra calculated using the finite-difference time-domain (FDTD) method (Figure 1(e)). A comparison of the extinction cross section spectra computed using the FDTD and coupled dipole methods is included in the Supporting Information showing close agreement (Figure S1).

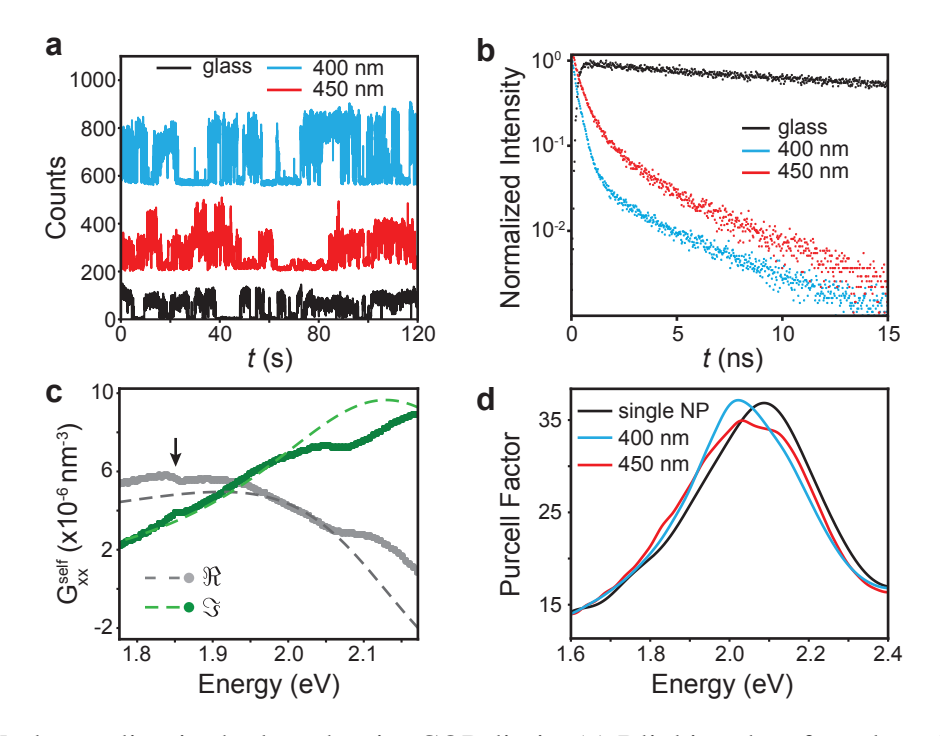


Figure 2: Weak coupling in the low-density CQD limit. (a) Blinking data from low-density CQD samples on glass (black) and inside the a=400 nm (blue) and a=450 nm (red) lattices. (b) Lifetime measurements of QDs on glass and within the NP arrays. (c) Comparison between the xx component of the complex-valued self-propagator \vec{G}^{self} for a QD displaced 10 nm radially from the center of an individual cylindrical NP (dashed lines) and from the central NP in an infinite lattice with 450 nm periodicity (dots). The black arrow indicates the energy of the Γ point SLR mode from Figure 1d. (d) Purcell factors calculated using the FDTD method for a single dipole emitter displaced 10 nm from an isolated Ag NP surface (black) and from the central NP in a finite array of 21x21 NPs with a=400 nm (blue) and a=450 nm (red). Deviations from the single NP Purcell spectra for the finite lattice systems coincide with features in the self-propagator spectra shown in panel (c).

Coupling between the SLRs and the synthesized CQDs (emission centered at 2.0 eV) was first investigated in the low-density limit. PL measurements were carried out on CQDs deposited on glass (no lattice), which exhibited blinking behavior indicative of a single CQD within the detection region (Figure 2(a) and Figures S2 and S3). Next, time-resolved PL measurements were

performed on CQDs placed inside the NP lattices (Methods section). The time traces in Figure 2(a) show blinking data collected from CQDs inside the a = 400 nm and a = 450 nm lattices (transmission spectra of the lattices used are presented in Figure S4) indicating the presence of one and two CQDs within the collection region, respectively. Time-resolved PL measurements were then performed on the fabricated glass and lattice samples to understand how the photonic environments of the lattices influence CQD spontaneous emission rates (Figure 2(b)). As expected for the weak coupling regime, the measured decay rates show significant reduction in the exciton lifetime due to Purcell enhancement for the CQDs placed within the NP lattices, and a transition from mono- to bi-exponential decay profiles was also observed. The measured decay profiles were fit to a multiexponential decay function to estimate Purcell factors for CQDs within each array (Supporting Information) yielding values ranging from 17 ± 2 to 60 ± 6 and 25 ± 3 to 80 ± 7 for the a = 400nm and a = 450 nm arrays, respectively. The uncertainties in the lifetime measurements inside the lattice are similar to the variation in the decay rates of pristine CQDs on glass (SI, figure S3), however the average Purcell factor varies for each CQD due to variation in the location of CQDs inside lattice relative to the NPs (Supporting Information). The magnitude of these enhancement values is nearly an order of magnitude larger than those reported in a related work studying emission enhancement of quantum emitters coupled to similar Ag NP arrays. ¹⁹ The emitters in that work were defect states in hexagonal boron nitride, which could not be reliably positioned in close proximity to NPs within the arrays. This limitation likely contributed to the lower Purcell factors reported in that work. In contrast, CQDs in this work were spin-coated onto the arrays and fluorescence mapping was used to identify regions with large PL enhancement. Given the spectral overlap of the SLR and single-NP LSPs, the plasmonic modes enabling the large Purcell factors demonstrated in Figure 2(b) could not be unambiguously identified from the transmission spectra.

A generalized Fano-Anderson model based on the coupled dipole method was developed to explicitly model the interaction between a single CQD and the SLR modes supported by the lattice. The CQD was approximated as a dipole moment \mathbf{d} with polarizability tensor $\boldsymbol{\beta}$ electromagnetically coupled to the LSP dipole moments \mathbf{p}_{mn} at each site of the lattice sites via their induced electric

fields, yielding the following system of equations

$$\mathbf{p}_{mn}(\omega) = \overset{\leftrightarrow}{\alpha}(\omega) \cdot \sum_{m'n'} \overset{\leftrightarrow}{\mathcal{G}}(\mathbf{r}_{mn}, \mathbf{r}_{m'n'}; k) \cdot \mathbf{p}_{m'n'}(\omega)$$

$$+ \overset{\leftrightarrow}{\alpha}(\omega) \cdot \overset{\leftrightarrow}{\mathcal{G}}(\mathbf{r}_{mn}, \mathbf{r}_{d}; k) \cdot \mathbf{d}(\omega)$$

$$\mathbf{d}(\omega) = \overset{\leftrightarrow}{\beta}(\omega) \cdot \sum_{mn} \overset{\leftrightarrow}{\mathcal{G}}(\mathbf{r}_{d}, \mathbf{r}_{mn}; k) \cdot \mathbf{p}_{mn}(\omega).$$
(1)

Here, $\overrightarrow{G}(\mathbf{r}_1, \mathbf{r}_2; k) = \frac{k^2}{\varepsilon_0 \varepsilon_r} \overrightarrow{G}(\mathbf{r}_1, \mathbf{r}_2; k)$ with \overrightarrow{G} the usual free-space Green function Dyadic weighted by the permittivity of free space ε_0 , the background dielectric constant ε_r , and photon wavenumber $k = \omega \sqrt{\epsilon_b}/c$. The primed sum signifies the omission of the self-interaction term. Solving Eq's (1) for the lattice-dressed eigenvalues of $\mathbf{d}(\omega)$ yields the following condition

$$\left[\stackrel{\leftrightarrow}{\boldsymbol{\beta}}(\omega)^{-1} - \frac{1}{\mathcal{A}_{BZ}} \iint_{BZ} dk^2 \stackrel{\leftrightarrow}{\boldsymbol{T}^*}_{\mathbf{k}} \cdot \stackrel{\leftrightarrow}{\boldsymbol{G}}_{\mathbf{k}}^{SLR} \cdot \stackrel{\leftrightarrow}{\boldsymbol{T}_{\mathbf{k}}}\right] \cdot \mathbf{d}(\omega) = \mathbf{0}. \tag{2}$$

The inverse of the term in the brackets is essentially the renormalized Green function of the CQD in the presence of the NP lattice. It depends on the lattice Green function $\overset{\leftrightarrow}{G}_{\mathbf{k}}^{\text{SLR}} = \left[\overset{\leftrightarrow}{\alpha}(\omega)^{-1} - \overset{\leftrightarrow}{S}_{\mathbf{k}}\right]^{-1}$, which determines the SLR band structure shown in Figures 1c,d. The lattice sum $\overset{\leftrightarrow}{S}_{\mathbf{k}}$ accounts for the interaction energy between the electromagnetically coupled LSPs, the interaction sum $\overset{\leftrightarrow}{T}_{\mathbf{k}}$ accounts for the interaction energy between the CQD and the SLR modes of the lattice with wavevector \mathbf{k} , and \mathcal{A}_{BZ} is the area of the Brillouin zone.

The Purcell factor characterizing the emission rate enhancement of an emitter in an inhomogeneous environment is $PF = 1 + \frac{6\pi\epsilon_0\epsilon_b}{k^3} Im(\hat{\mathbf{n}}_d \cdot \overrightarrow{\mathbf{G}}^{\text{self}} \cdot \hat{\mathbf{n}}_d)$, where the self-propagator $\overrightarrow{\mathbf{G}}^{\text{self}}$ represents the retarded field emitted by the dipole \mathbf{d} that arrives back at its own position \mathbf{r}_d after scattering off of the NPs in the lattice. For the case of a CQD placed 10 nm along $\hat{\mathbf{x}}$ from the NP surface, and oriented along the same direction, the real and imaginary parts of

$$\overrightarrow{\boldsymbol{G}}_{SLR}^{self} = \frac{1}{\mathcal{A}_{BZ}} \iint_{BZ} dk^2 \, \overrightarrow{\boldsymbol{T}}_{\mathbf{k}}^* \cdot \overrightarrow{\boldsymbol{G}}_{\mathbf{k}}^{SLR} \cdot \overrightarrow{\boldsymbol{T}}_{\mathbf{k}}$$
(3)

calculated using this approach for the a=450 nm lattice are quite similar to those obtained if only the nearest NP to the CQD is present (Figure 2c), with only a small feature near 1.85 eV due to the Γ point lattice mode (indicated by the black arrow). This behavior is supported by fully numerical evaluation of the Purcell factors for identical system geometries calculated using the FDTD method for finite lattice systems with 441 NPs (Figure 2d). The Purcell factor spectra for each lattice largely follow those of the single-NP response, showing small deviations corresponding to strong features in the SLR band structures (Figure 1 c,d). The magnitude of the calculated PFs obtained for a 10 nm displacement from the NP surface are similar to those extracted from the time-resolved PL measurements in Figure 2b. Small deviations are expected due to the uncertainty in the NP location relative to the NP surface in the experiments. Our model demonstrates that individual emitters couple to the LSP modes supported by the nearest NP rather than to the delocalized SLR modes, which is consistent with other recent works investigating weak coupling between plasmonic lattices and individual emitters. 19,45,46

Turning now to a consideration of the influence of higher QD concentrations, we first note that the value of the coupling energy $\hbar\Omega_g$ between a cavity and a system of N quantum emitters, which determines whether the combined system is in the weak, intermediate, or strong coupling regime, is given by 47 $\hbar\Omega_g = \int \mu_{\rm eff}(\mathbf{r}) \cdot \mathbf{E}_{\rm SLR}(\mathbf{r}) d^3 r$. In this expression $\mu_{\rm eff}(\mathbf{r})$ is a position-dependent effective dipole moment density (*i.e.* polarization) of the QE system and $\mathbf{E}_{\rm SLR}$ represents the local vacuum fluctuations of the SLR field. 48 Based on past work, we expect this coupling to be proportional to \sqrt{N} . 2,49 The eigenstate energies of the upper (U) and lower (L) polariton branches of the coupled light-matter system are thus given by 47

$$\hbar\omega_{\text{U/L}} = \frac{\hbar}{2} \left(\omega_{\text{CQD}} + \omega_{\text{SLR}} - i(\gamma_{\text{CQD}} + \gamma_{\text{SLR}}) \right) \\
\pm \sqrt{\left(\Delta + i(\gamma_{\text{CQD}} - \gamma_{\text{SLR}})\right)^2 + 4\Omega_g^2}, \tag{4}$$

where $\Delta = \omega_{SLR} - \omega_{CQD}$ is the detuning between the uncoupled CQD and SLR frequencies. In the case of zero detuning, the strong coupling regime is realized when the square root term in eq. (4) is

real-valued, *i.e.* when $\Omega_g > \frac{|\gamma_{\rm QD} - \gamma_{\rm SLR}|}{2}$. The weak electromagnetic coupling between the SLR modes and low-density CQD ensembles can therefore be understood as arising from the spatial mismatch between the localized emission of the individual CQDs and the delocalized SLR modes supported by the NP array, which reduces the value of $\hbar\Omega_g$. The coupling between these two systems can be increased using high-density CQD ensembles such that many CQDs are excited within each unit cell inside the excitation region.

This strategy was first pursued for the a=400 nm array. Three high-density CQD assemblies were synthesized comprising CQDs of different sizes in order to achieve positive, negative and near-zero detuning Δ between the CQD emission (PL maximum) and the Γ point SLR of the a=400 nm lattice (Figure 3(a)). The measured PL spectra of the hybrid CQD-SLR samples are presented in Figure 3(b) for CQD concentrations of 142 mM. The emission from the CQD₁ sample was significantly red-detuned from the Γ point SLR and remained a single-peak once placed inside the NP array. The small blue-shift was likely caused by preferential Purcell enhancement of the PL on the blue side of the emission due to the Γ point SLR detuning. The PL spectrum of the CQD₂-SLR sample ($\Delta \approx 0$), however, exhibited a clear split-peak structure – the characteristic signature of the strong coupling regime. Although the emission from the CQD₃ sample was slightly blue-detuned from the Γ point SLR, there was still significant spectral overlap and a similar two-peak spectral profile was observed for the CQD₃-SLR system.

While the change in the CQD PL in Figure 3 from a one- to two-peak structure following introduction into the lattice is indicative of the formation of upper and lower polariton states in the strong coupling regime, further insight can be gained from the dependence of the PL lineshapes on the CQD density (Supporting Information). Provided $\Delta = 0$ and the SLR and CQD resonance frequencies are large compared to the respective damping rates, Eq. (4) predicts that the energy splitting between the upper and lower polariton branches is proportional to $\sqrt{N/V}$, where N is the number of emitters within the SLR mode volume V. The proper definition of the mode volume in lossy plasmonic systems has, however, been the subject of recent debate and it is often difficult or impossible to accurately determine N experimentally. We approximate N/V as the concentration

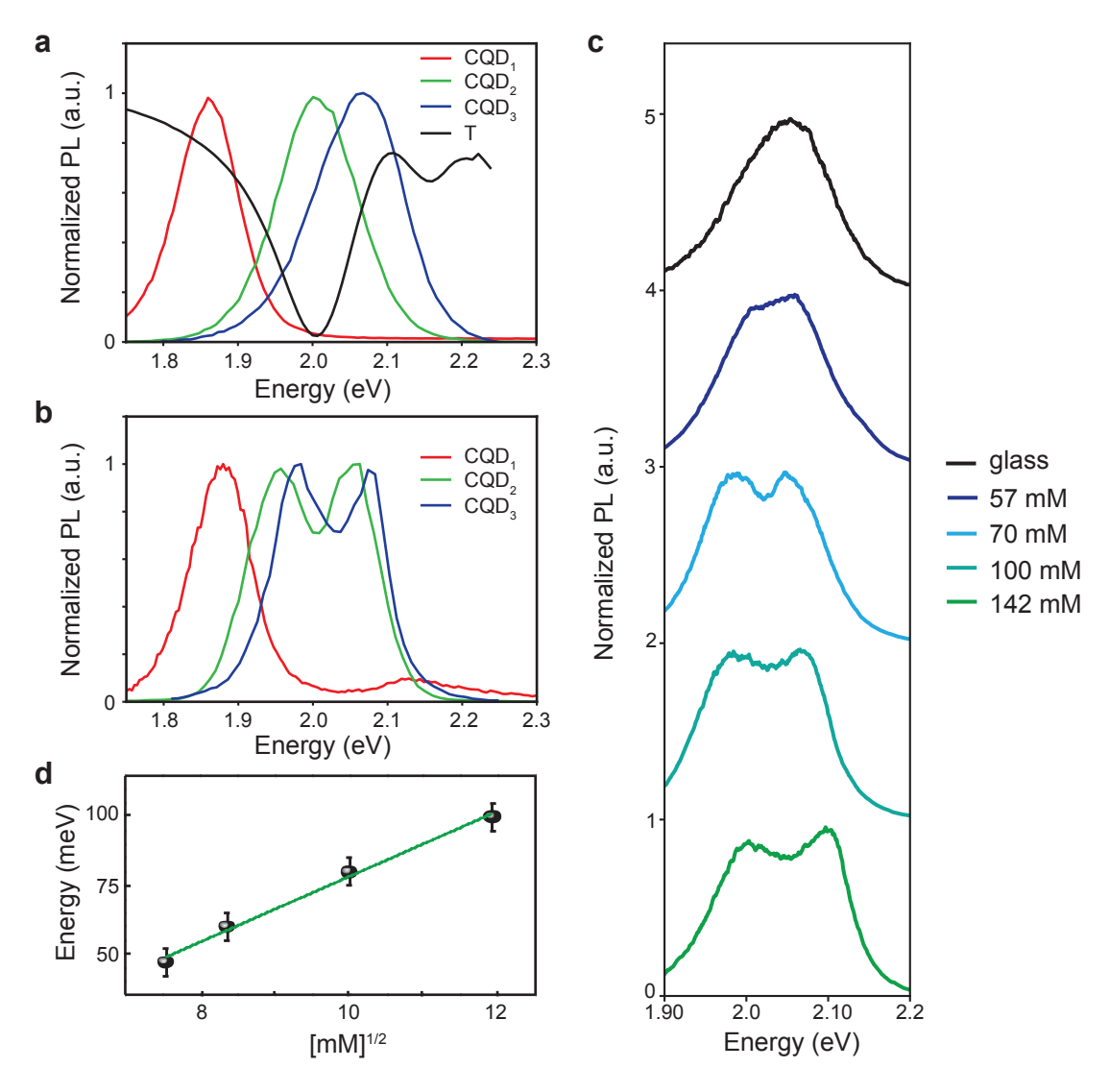


Figure 3: CQD ensemble coupling to Γ point SLR of 400 nm lattice. a) Normalized PL spectra of fabricated CQD_i samples (i = 1, 2, 3) on glass. The Γ point transmission spectrum of the a = 400 nm lattice from Figure S4 is shown in black. b) Normalized PL spectra of the CQD_i samples in panel (a) following introduction into the plasmonic lattice. c) Evolution of the PL lineshape for increasing concentration of CQD₂. Each trace has been offset by one unit for clarity. d) Extracted peak energy splitting from panel (c) plotted against the square root of the CQD concentration.

of emitters in the experiment, which has recently been shown to be a good approximation for open plasmonic systems where the emitters are distributed over an extended region surrounding the NPs. ⁵⁰ Figure 3(c) shows the evolution of the CQD₂ PL from a one- to two-peak structure as the CQD density inside the lattice was increased from 57 mM to 142 mM. By fitting the measured PL spectra to a sum of two Gaussians to extract the energies of the new modes, the measured energy splitting between the observed peaks as a function of the square root of the CQD concentration yielded a straight line (Figure 3(d)). This observed dependence further supports the interpretation of the the PL evolution in terms of a strong coupling picture.

The number of CQDs is too large in the high-density limit to explicitly track every degree of freedom as was done above for the case of a single CQD. Instead, the CQD assembly is treated as a homogeneous effective medium with a dielectric function given by

$$\frac{\epsilon(\omega)}{\epsilon_0} = \epsilon_b + \frac{f\omega_{\text{CQD}}^2}{\omega_{\text{CQD}}^2 - \omega^2 - i\omega\gamma_{\text{CQD}}}.$$
 (5)

Here, the oscillator strength f determines how strongly the background dielectric ϵ_b is modified by the frequency-dependent Lorentzian response of the CQD layer, and encapsulates the density of CQDs used in the experiments. Since the dipolar lattice Green function depends on the lattice sum and the single-NP polarizability, ¹⁷ Eq. (5) must be included in both $\overrightarrow{S}_{\mathbf{k}}(\omega)$ and $\overrightarrow{\alpha}(\omega)$. Modelling the NPs as Ag nanospheres of 50 nm radius allows Eq. (5) to be simply integrated into the analytic form of the nanosphere polarizability. ⁵¹ As the oscillator strength f is increased, the imaginary part of the Mie polarizability splits into a double-peak structure, with a minimum at ω_{CQD} (Figure 4a), signaling the onset of strong coupling between the single-NP LSP and the surrounding CQD medium.

In order to understand the CQD-NP array PL in the high-density limit, we introduce the wave vector-resolved lattice density of states

$$\rho(\omega, \mathbf{k}_{\parallel}) \propto \text{Tr}\left[\text{Im}\left(\stackrel{\leftrightarrow}{\mathcal{G}}_{SLR}(\omega, \mathbf{k}_{\parallel})\right)\right],$$
(6)

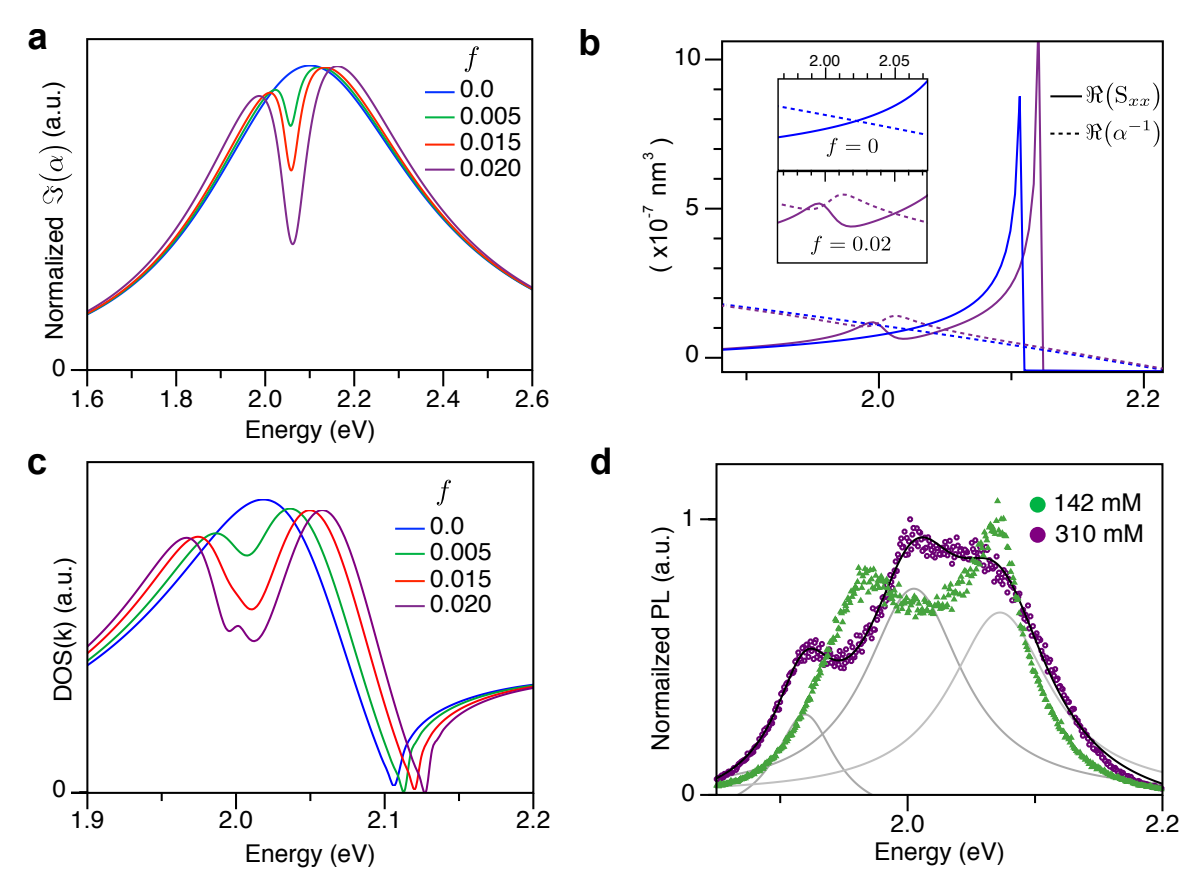


Figure 4: Effective medium model for CQD-SLR coupling in the high-density limit. (a) Imaginary part of the spherical NP Mie polarizability for different values of the CQD medium oscillator strength illustrating the onset of strong coupling between individual NPs and the CQD medium. (b) Real parts of the inverse polarizability (dashed) and the lattice sum (solid) in the absence of any CQDs (blue) showing a single intersection point. Purple traces represent the same quantities at high CQD concentrations corresponding to f = 0.02 in eq. (5). Insets present close-up views of where intersections occur. (c) Wave vector-resolved density of states at the Γ point of the a = 400 nm periodicity lattice as a function of the CQD oscillator strength showing the evolution from one, to two, to three peaks. d) Experimental PL spectra for medium- (green) and high-density (purple) CQD assemblies showing the transition from two to three peaks. The experimental data was fit to a three-Lorentzian function (black) with the individual Lorentzian contributions shown in grey.

which can be used to recover the local density of states by integrating $\rho(\omega, \mathbf{k}_{\parallel})$ over the Brillouin zone. While previous works have employed similar coupled dipole treatments to understand strong coupling in high-density QE-SLR systems, ⁴⁰ only the modification of NP polarizability by the QE medium was considered. The presence of the QDs is also accounted for, here, in the evaluation of the lattice sum (Figure 4b). Features appear in the lattice spectra at energies close to where $\operatorname{Re}(\overset{\leftrightarrow}{\alpha}^{-1}) = \operatorname{Re}(\overset{\leftrightarrow}{S}_{k})$, since this occurs nearby the poles of the lattice Green function $\overset{\leftrightarrow}{\mathcal{G}}_{SLR}$. Due to the symmetry of the lattice, $\rho_{xx}(\omega, \mathbf{k}_{\parallel}) = \rho_{yy}(\omega, \mathbf{k}_{\parallel})$ at the Γ point, while the zz component describes z-oriented dipoles that do not radiate into the far-field normal to the lattice plane. The spectrum of $\rho_{xx}(\omega, \mathbf{k}_{\parallel})$ at the Γ point is presented in Figure 4c for different values of the oscillator strength f in eq. (5). As expected, the evolution of the peak structure matches that of the intersections illustrated in Figure 4b as the CQD oscillator strength is increased from f = 0 (blue) to f = 0.015. The similar evolution between $\rho_{xx}(\omega,\mathbf{k}_{\parallel}=0)$ shown in 4c with the measured density-dependent splitting behavior in Figure 3 supports a strong coupling interpretation. We also note that since the oscillator strength is proportional to concentration, the \sqrt{N} dependence can also be recovered in this analysis. The analysis presented above has important consequences for understanding the underlying dynamics of these systems as it shows that strong coupling between the CQD medium and single NP occurs in concert with strong coupling between the CQD medium and the collective SLR modes of the lattice.

When the oscillator strength is increased above $f \sim 0.015$, the real parts of the inverse polarizability and the lattice sum intersect at three points (Figure 4b), which indicates the existence of three modes that are manifest in the peak structure of $\rho_{xx}(\omega, \mathbf{k}_{\parallel} = 0)$ (Figure 4c). We see that this behavior is confirmed experimentally in the PL spectrum when the CQD concentration was increased to 310 mM (Figure 4d), as a third peak is found near the frequency of the uncoupled CQD emission. A fit to three Lorentzians is included in Figure 4d and the fit parameters are tabulated in the Supporting Information. This behavior is qualitatively reproduced in FDTD calculations of the transmission spectra of light incident on a = 400 nm periodicity arrays of Ag NPs with the same dimensions as used in Figure 1 embedded in a 60 nm thick effective medium slab as a function of f

(Figure 5a). Additional details related to the FDTD calculations and effective medium parameters are included in the Supporting Information.

Before discussing the physical nature of the third peak, it should be noted that while peak splitting evident in $\rho_{xx}(\omega, \mathbf{k}_{\parallel})$ (itself proportional to extinction, Figure 4c), the experimental PL spectrum (Figure 4d), and the simulated transmission spectra (Figure 5a) are suggestive of strong coupling, work done on single NP-emitter hybrid systems suggests that in contrast to extinction and scattering spectra (which the above are proportional to), the onset of splitting in the absorption spectrum typically requires higher values of f. Thus, it has been suggested that interaction-induced peak-splitting in the absorption spectrum constitutes a more robust criteria for determining if a nanosystem has reached the strong coupling regime. 52,53 To determine if this criterion is met in our system, position-dependent absorption spectra were calculated at the four locations shown in Figure 5b. In Figure 5c, the absorption spectra calculated at these points for the coupled system (i.e. lattice + effective medium, colored traces) are compared against the absorption spectra of the bulk effective medium materials in the absence of the NP array (proportional to $\text{Im}[\epsilon_m(f)]$, grey). As expected, at position N1 just outside of the NP and in the plasmonic hot spot, the absorption spectrum exhibits f-dependent splitting about the uncoupled emitter frequency (first column of Figure 5c).

Examining the position-dependent absorption can also elucidate the nature of the third peak observed in Figures 4c, d, and 5a. In agreement with those results, Figure 5 shows that increasing the oscillator strength in the FDTD simulation to f = 0.03 and above induces the emergence of a third mode near the energy of the uncoupled emitters (\sim 2 eV Figure 5c). Similar phenomena have been reported previously for both isolated NP-emitter systems and lattice systems consisting of excitons in TMDC multi-layers coupled to 2D Ag NP arrays. 52,54,55 In both systems, it was reported that the it is the emitters located predominantly within the near-field of the NPs that strongly couple with the LSPs to give the two Rabi-split peaks, while the emitters located beyond the influence of the plasmonic near-field contribute to the formation of the third peak. The three far-field positions selected for Figure 5c are positioned near an anti-node of the uncoupled cavity

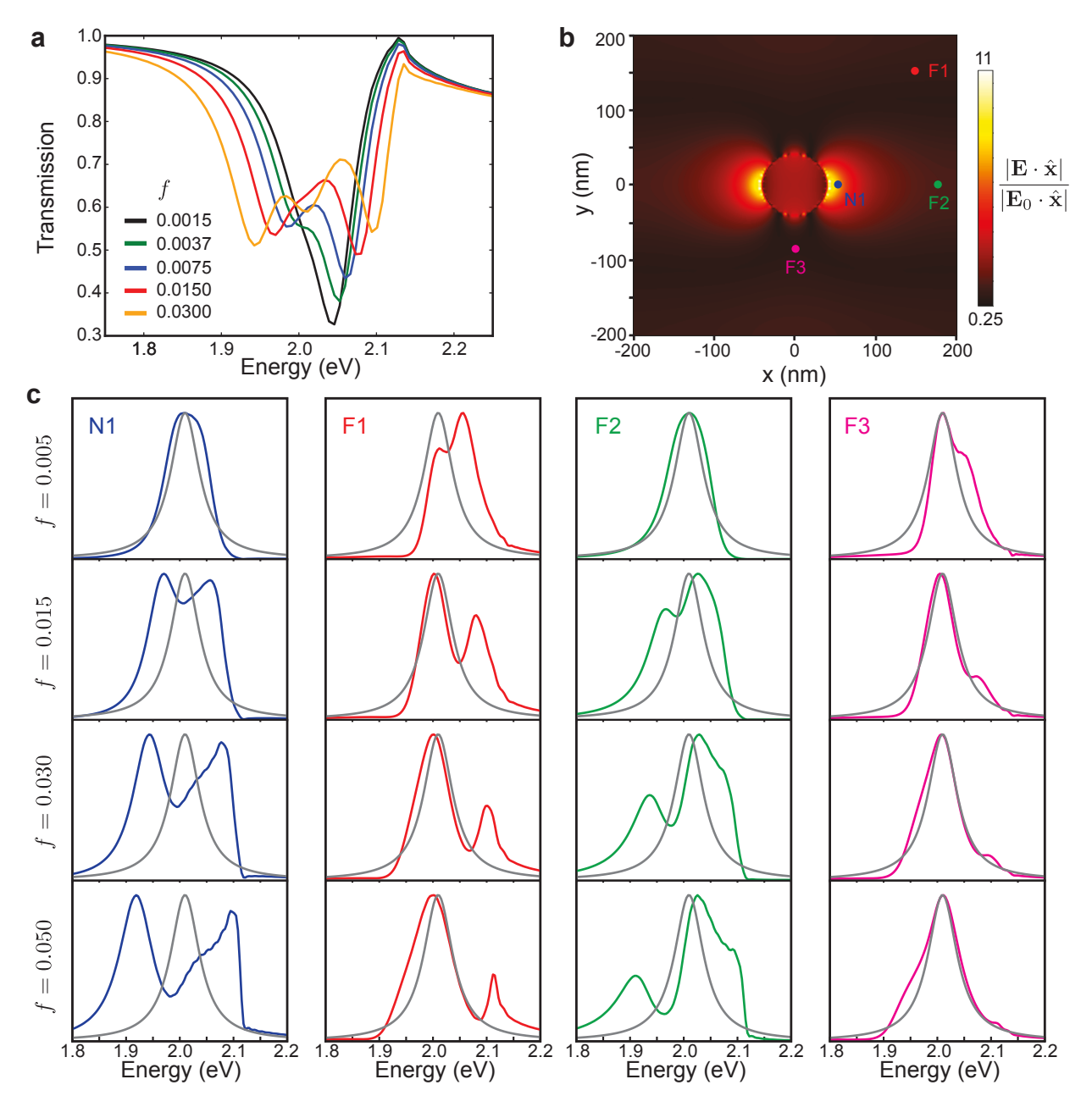


Figure 5: Position-Dependent Absorption Within Ag Array Unit Cell. a) Transmission spectra calculated using FDTD of a=400 nm periodicity array embedded in a 60 nm thick effective medium slab as a function of the oscillator strength f. b) $|E_x|$ normalized by the incident field magnitude within a unit cell of the array in (a) with f=0.03 excited at normal incidence at 1.94 eV. The colored markers indicate x,y positions (z=0) where the absorption spectra are calculated. c) Absorption spectra at points within the unit cell marked in panel (b) as a function of the effective medium oscillator strength f.

field (F1), a node of the uncoupled cavity field (F2), and a node of the interacting system (F3). In contrast to the case of the single NP, as well as to the previous lattice study, the *f*-dependent absorption spectra at the far positions in Figure 5 display a position-dependent splitting dictated by the spatial profile of the electric field of the interacting system. The importance of the plasmonic NPs is further evidenced by disappearance of the splitting in the absorption spectrum at position N1 when the NP material is Ti rather than Ag (Supporting Information).

The three peak structure observed in this paper is thus a superposition of both the strong coupling peak structure most evident in the near-field, and the SLR-mediated enhanced absorption near the uncoupled resonance frequency of the effective medium. Notably, both in terms of strong coupling and enhanced absorption, one of the key lattice-driven effects is to reduce the required density of emitters by approximately a factor of 10.⁵² Further, unlike what has been reported in previous work on lattices, and also at the single particle level, strong coupling is observed at positions far outside the plasmonic near-field. Interestingly, while coupled oscillators are often invoked to phenomenologically model the splitting of upper and lower polaritons in the strong coupling regime, these models are incapable of capturing the emergence of this collective emitter mode, ⁵⁵ which appears naturally in the coupled dipole model presented here for sufficiently large CQD oscillator strengths.

Conclusion

We have presented experimental measurements investigating the coupling between low- and high-density CQD ensembles and plasmonic NP arrays, which were interpreted with the help of analytical and numerical calculations. In the low-density limit, PL measurements and Purcell factor calculations indicate CQDs are weakly coupled to individual NPs rather than to the delocalized SLR modes of the NP array. In the high-density limit, coupling between CQD ensembles and Γ point SLRs leads to density-dependent mode splitting characteristic of the formation of upper and lower polariton states in the strong coupling regime. At still higher emitter concentrations, an

additional mode is observed that is attributed to emission from a collective emitter state mediated by the SLR field. Our work extends the study of strong coupling between plasmonic SLRs and quantum emitters to a separate class of colloidal QD emitters and highlights the density-dependent transition from localized to delocalized coupling.

Methods

Fabrication of Ag NP lattices: Ag NP lattices were fabricated with a soft nanofabrication process called PEEL (photolithography, etching, electron-beam deposition and lift-off). 56 A poly(dimethylsiloxane) mask with square lattice spacing a = 400 nm was used in phase-shift photolithography to produce photoresist posts with diameter d = 130 nm on Si (100) wafers. Then, 10 nm of chromium (Cr) was deposited on the substrates by thermal evaporation, followed by the removal of the photoresist posts to produce Cr hole arrays. Using the Cr hole array as a mask, Si holes were then created by deep reactive-ion etching. An Au hole array with a smaller NP diameter d = 80 nm was obtained by depositing 100 nm of Au on the Cr-Si hole array. After etching the Cr layer, the Au hole mask was floated on the surface of distilled water and transferred to a glass substrate. Ag NPs were produced by thermal evaporation through the Au hole-array mask and the Au mask was then removed using scotch tape. A 2 nm Cr layer was deposited in-between for better adhesion between the Ag NPs and the glass substrate.

Synthesis of graded CdSe/ZnS CQDs: Graded CdSe/ZnS core/shell CQDs were prepared using a chemical synthesis method. Cadmium oxide (CdO) (25.68 mg), zinc oxide (ZnO) (162mg), ODE (10 ml) and olaic acid (3.52 ml) were loaded into a 25 ml three-neck flask and heated to 110°. After degasing the flask for 20 min, the flask was filled with nitrogen gas and heated to 310° C until the solution turned clear. Selenium (Se) and sulphur (S) precursor were prepared by dissolving Se (20.5mg) and S (85mg) in 2 ml TOP. 1.5 ml of the Se-S-TOP precursor was added into the three neck flask at 300° C for QD growth. The QD size was controlled using the reaction time, which was stopped by placing the three neck flask in a water bath. The CQDs were precipitated using

acetone. The CQD solution was further cleaned by chloroform:methanol (1:3) ratio *via* centrifuge at 12000 rpm. Photoluminescence and absorption spectra of cleaned QDs are included in Figure S2 of the Supporting Information. Finally, CQDs were dispersed in toluene for spin coating. CQD concentrations were determined by measuring the CQD weight after evaporation of the toluene solvent.

Preparation of hybrid CQD-plasmonic lattice samples: In the low-density limit, CQDs were deposited on the fabricated NP lattices by spin-coating 1 nM solutions of CQDs in PMMA (1 mg/mL). The high-density CQD-plasmonic lattice samples were prepared by spin-coating solutions of CQDs in toluene onto the NP lattices at 3000 rpm for one minute. The concentrations of the CQD solutions were varied as described in the main text.

Blinking and time-resolved photoluminescence measurements in the low-density CQD limit: Isolated CQDs were located by fluorescence mapping using a Pico-Quant inverted microscope. CQDs were excited by focusing a 509 nm (2.435 eV) wavelength, 1 MHz repetition rate, $0.1 \,\mu\text{W}$ pulsed laser using an oil immersion 100X objective (NA = 1.06) in an inverted microscope. The emission was collected using the same objective and detected with a single-photon avalanche diode (SPAD). TRPL measurements were performed on sample locations where the observed fluorescence blinking was indicative of individual CQDs within the excitation/collection region.

Photoluminescence measurements in the high-density CQD limit: PL measurements of high-density CQD assemblies inside the NP lattices were performed using the Witec system. ⁵⁷ CQD assemblies were excited by focusing 514 nm (2.41 eV) CW laser light using a 10X objective (NA = 0.20), and the emission was collected through the same objective in far-field reflection mode. The collected light was filtered using a low-pass filter (520 nm cutoff) to block the excitation light from reaching the detector.

Coupled Dipole Method: Two dimensional lattices are defined by basis vectors \mathbf{a}_1 and \mathbf{a}_2 such that each lattice site can be expressed as $\mathbf{r}_{mn} = m \ \mathbf{a}_1 + n \ \mathbf{a}_2$, with $m, n \in \mathbb{Z}$. Within the coupled dipole approximation, the normalized extinction efficiency associated with a plane wave polarized

along $\hat{\mathbf{n}}$ incident on a periodic array of NPs with polarizability $\overset{\leftrightarrow}{\alpha}$ is

$$\sigma_{\text{ext}}(\omega, \mathbf{k}_{\parallel}) = \frac{k}{\pi R^2 \epsilon_r \epsilon_0} \text{Im} \left(\hat{\mathbf{n}} \cdot \left[\stackrel{\leftrightarrow}{\alpha} (\omega)^{-1} - \stackrel{\leftrightarrow}{S} (\omega, \mathbf{k}_{\parallel}) \right]^{-1} \cdot \hat{\mathbf{n}} \right), \tag{7}$$

where R is the cylindrical NP radius and $k = 2\pi \sqrt{\epsilon_r}/\lambda$ is the magnitude of the wave vector in the surrounding medium characterized by the dielectric function ϵ_r . The so-called lattice sum is defined by

$$\overset{\leftrightarrow}{\mathbf{S}}_{\mathbf{k}} = \overset{\leftrightarrow}{\mathbf{S}}(\omega, \mathbf{k}_{\parallel}) = \frac{k^2}{\epsilon_r \epsilon_0} \sum_{m'n' \neq 0} \overset{\leftrightarrow}{\mathbf{G}}(\mathbf{0}, \mathbf{r}_{m'n'}, \omega) e^{-i\mathbf{k}_{\parallel} \cdot \mathbf{r}_{m'n'}}, \tag{8}$$

where \mathbf{k}_{\parallel} is the in-plane momentum of a particular Bloch mode and $\overset{\leftrightarrow}{G}$ is the free space Green dyadic given by

$$\overrightarrow{G}(\mathbf{r}_{i}, \mathbf{r}_{j}, \omega) = \left[\left(1 + \frac{i}{kR_{ij}} - \frac{1}{(kR_{ij})^{2}} \right) \overrightarrow{\mathbf{I}} + \left(-1 - \frac{3i}{kR_{ij}} + \frac{3}{(kR_{ij})^{2}} \right) \hat{\mathbf{R}}_{ij} \hat{\mathbf{R}}_{ij} \right] \frac{e^{ikR_{ij}}}{4\pi R_{ij}}.$$
(9)

In this expression, $R_{ij} = |\mathbf{r}_i - \mathbf{r}_j|$, $\hat{\mathbf{R}}_{ij} = (\mathbf{r}_i - \mathbf{r}_j)/R_{ij}$, and $\hat{\mathbf{R}}_{ij}\hat{\mathbf{R}}_{ij}$ represents the dyadic product. The interaction sum appearing in the definition of $\overset{\leftrightarrow}{G}_{\text{SLR}}$ is defined as

$$\overset{\leftrightarrow}{T}_{\mathbf{k}} = \overset{\leftrightarrow}{T}(\mathbf{r}, \omega, \mathbf{k}_{\parallel}) = \frac{k^2}{\epsilon_r \epsilon_0} \sum_{m'n'} \overset{\leftrightarrow}{G}(\mathbf{r}, \mathbf{r}_{m'n'}, \omega) e^{i\mathbf{k}_{\parallel} \cdot (\mathbf{r} - \mathbf{r}_{m'n'})}.$$
(10)

The lattice and interaction sums were efficiently and accurately evaluated using Ewald's method. 58,59

Accurate polarizability tensors were determined numerically in a separate step for cylindrical NPs with the same geometric parameters as those used in the experiments. To do this, the scattered field \mathbf{E}_s produced by an isolated cylinder excited by plane wave was first calculated using the boundary-element method.⁶⁰ A multipole decomposition was performed using \mathbf{E}_s at each frequency to evaluate the expansion coefficient values for a representation of the scattered field in terms of vector spherical harmonics.⁶¹ The extracted a_1 scattering coefficient is related to the

polarizability tensor element along the direction of the incident polarization $\hat{\bf n}$ by ⁵¹

$$\alpha_{\hat{\mathbf{n}}\hat{\mathbf{n}}} = i \frac{6\pi\epsilon_r \epsilon_0}{k^3} a_1. \tag{11}$$

The full polarizability tensor $\overset{\leftrightarrow}{\alpha}$ is constructed by repeating the multipole decomposition procedure for $\hat{\bf n}$ along the long and short cylinder axes.

Finite-Difference Time-Domain Simulations: Purcell factor calculations based on the extended coupled dipole Fano-Anderson model were verified via fully numerical solution of Maxwell's equations using the finite-difference time-domain method implemented by Lumerical. The interaction between a single CQD and the NP array was approximated by placing a single dipole source 10 nm from the edge of the central NP along the $\hat{\mathbf{x}}$ direction (and oriented along the same direction) in a 21 x 21 finite array enclosed by PML absorbing boundary conditions on all sides of the simulation region. The mesh accuracy setting was set to 6, and a mesh override region with 1x1x1 nm resolution was used over the volume containing the central NP and the dipole emitter. Additional simulations for varying numbers of NPs in the finite arrays confirmed that 21×21 NPs is large enough to avoid spurious edge effects arising from the use of a finite, rather than infinite, lattice.

Position-dependent absorption spectra presented in Figure 5 were calculated as 62

$$\sigma_{\text{abs}} = \frac{1}{N} \omega \operatorname{Im}[\epsilon_m(\omega)] |\mathbf{E}|^2, \tag{12}$$

where N is a position-dependent normalization constant, and $\epsilon_m(\omega)$ is given by Eq. (5).

Supporting Information

Comparison of lattice extinction spectra calculated using FDTD and coupled dipole methods, absorption and photoluminescence spectra of CQDs, additional details regarding fluorescence mapping and time-resolved photoluminescence measurements, transmission spectrum of plasmonic lattice used for CQD measurements, determination of experimental Purcell factors, high-density

CQD sample preparation, peak splitting as a function of CQD film absorbance, additional FDTD simulation results with effective medium model for the CQD thin film. The Supporting Information is available free of charge online.

Acknowledgement

The authors acknowledge the Indo-U.S. Science Technology Forum (IUSSTF) for funding through a virtual centre on quantum plasmonics. The authors acknowledge DST Nanomission, India for funding. GCS and CC were supported by NSF grant CHE-1760537 (theory development), and GCS, MB, and TO were supported by NSF grant DMR-1904385 (theory applications and laser research). This work utilized the Northwestern University Micro/Nano Fabrication Facility (NU-FAB), which is partially supported by Soft and Hybrid Nanotechnology Experimental (SHyNE) Resource (NSF ECCS-1542205), the Materials Research Science and Engineering Center (DMR-1720139), the State of Illinois, and Northwestern University. This research was supported in part by the Quest high performance computing facility at Northwestern University, which is jointly supported by the Office of the Provost, the Office for Research, and Northwestern University Information Technology.

Author Contributions

MB and CC wrote the bulk of the manuscript and prepared all figures. RKY synthesised the CQDs and preformed all the experiments on the SLR-CQD systems. MB and CC conceived of and carried out the coupled dipole calculations for the single QE-SLR system. MB implemented the numerical solution and performed FDTD simulations of the dipole emitter coupled to finite NP arrays. CC conceived of and calculated the effective medium extension of the coupled dipole model for the strong coupling regime. We fabricated the original NP lattices used in the CQD-SLR measurements, and XR fabricated and measured the transmission properties of the lattices presented in Figure 1. GCS, TWO, and JKB guided the theoretical and experimental investigations.

All authors commented on and revised the manuscript.

References

- (1) Delga, A.; Feist, J.; Bravo-Abad, J.; Garcia-Vidal, F. Quantum Emitters Near a Metal Nanoparticle: Strong Coupling and Quenching. *Phys. Rev. Lett.* **2014**, *112*, 253601.
- (2) Törmä, P.; Barnes, W. L. Strong Coupling Between Surface Plasmon Polaritons and Emitters: a Review. *Rep. Prog. Phys.* **2014**, *78*, 013901.
- (3) Hsu, L.-Y.; Ding, W.; Schatz, G. C. Plasmon-Coupled Resonance Energy Transfer. *J. Phys. Chem. Lett.* **2017**, *8*, 2357–2367.
- (4) Shahbazyan, T. V. Cooperative Emission Mediated by Cooperative Energy Transfer to a Plasmonic Antenna. *Phys. Rev. B* **2019**, *99*, 125143.
- (5) Guebrou, S. A.; Symonds, C.; Homeyer, E.; Plenet, J.; Gartstein, Y. N.; Agranovich, V. M.; Bellessa, J. Coherent Emission from a Disordered Qrganic Semiconductor Induced by Strong Coupling with Surface Plasmons. *Phys. Rev. Lett.* 2012, 108, 066401.
- (6) Otten, M.; Larson, J.; Min, M.; Wild, S. M.; Pelton, M.; Gray, S. K. Origins and Optimization of Entanglement in Plasmonically Coupled Quantum Dots. *Phys. Rev. A* **2016**, *94*, 022312.
- (7) Hoang, T. B.; Akselrod, G. M.; Mikkelsen, M. H. Ultrafast Room-Temperature Single Photon Emission from Quantum Dots Coupled to Plasmonic Nanocavities. *Nano Lett.* **2015**, *16*, 270–275.
- (8) Tiecke, T.; Thompson, J. D.; de Leon, N. P.; Liu, L.; Vuletić, V.; Lukin, M. D. Nanophotonic Quantum Phase Switch with a Single Atom. *Nature* **2014**, *508*, 241–244.
- (9) Gonzalez-Tudela, A.; Martin-Cano, D.; Moreno, E.; Martin-Moreno, L.; Tejedor, C.; Garcia-Vidal, F. Entanglement of Two Qubits Mediated by One-Dimensional Plasmonic Waveguides. Phys. Rev. Lett. 2011, 106, 020501.

- (10) Hubert, C.; Rumyantseva, A.; Lerondel, G.; Grand, J.; Kostcheev, S.; Billot, L.; Vial, A.; Bachelot, R.; Royer, P.; Chang, S.-h.; Gray, S. K.; Wiederrecht, G. P.; Schatz, G. C. Near-Field Photochemical Imaging of Noble Metal Nanostructures. *Nano Lett.* **2005**, *5*, 615–619.
- (11) Hoang, T. B.; Akselrod, G. M.; Yang, A.; Odom, T. W.; Mikkelsen, M. H. Millimeter-Scale Spatial Coherence from a Plasmon Laser. *Nano Lett.* **2017**, *17*, 6690–6695.
- (12) Groß, H.; Hamm, J. M.; Tufarelli, T.; Hess, O.; Hecht, B. Near-Field Strong Coupling of Single Quantum Dots. *Sci. Adv.* **2018**, *4*, eaar4906.
- (13) Tame, M. S.; McEnery, K.; Özdemir, Ş.; Lee, J.; Maier, S.; Kim, M. Quantum Plasmonics. *Nat. Phys.* **2013**, *9*, 329340.
- (14) Manjavacas, A.; Garcia de Abajo, F. J.; Nordlander, P. Quantum Plexcitonics: Strongly Interacting Plasmons and Excitons. *Nano Lett.* **2011**, *11*, 2318–2323.
- (15) Zhao, L.; Kelly, K. L.; Schatz, G. C. The Extinction Spectra of Silver Nanoparticle Arrays: Influence of Array Structure on Plasmon Resonance Wavelength and Width. *J. Phys. Chem.* B 2003, 107, 7343–7350.
- (16) Wang, W.; Ramezani, M.; Väkeväinen, A. I.; Törmä, P.; Rivas, J. G.; Odom, T. W. The Rich Photonic World of Plasmonic Nanoparticle Arrays. *Mater. Today* 2018, 21, 303– Theory of Strong Coupling Between314.
- (17) Cherqui, C.; Bourgeois, M. R.; Wang, D.; Schatz, G. C. Plasmonic Surface Lattice Resonances: Theory and Computation. *Acc. Chem. Res.* **2019**, *52*, 2548–2558.
- (18) Guo, R.; Hakala, T. K.; Törmä, P. Geometry Dependence of Surface Lattice Resonances in Plasmonic Nanoparticle Arrays. *Phys. Rev. B* **2017**, *95*, 155423.
- (19) Tran, T. T.; Wang, D.; Xu, Z.-Q.; Yang, A.; Toth, M.; Odom, T. W.; Aharonovich, I. Deterministic Coupling of Quantum Emitters in 2D Materials to Plasmonic Nanocavity Arrays. Nano Lett. 2017, 17, 2634–2639.

- (20) Zhou, W.; Dridi, M.; Suh, J. Y.; Kim, C. H.; Co, D. T.; Wasielewski, M. R.; Schatz, G. C.; Odom, T. W. Lasing Action in Strongly Coupled Plasmonic Nanocavity Arrays. *Nat. Nanotechnol.* 2013, 8, 506511.
- (21) Yang, A.; Hoang, T. B.; Dridi, M.; Deeb, C.; Mikkelsen, M. H.; Schatz, G. C.; Odom, T. W. Real-Time Tunable Lasing from Plasmonic Nanocavity Arrays. *Nat. Commun.* **2015**, *6*, 6939.
- (22) Hakala, T.; Rekola, H.; Väkeväinen, A.; Martikainen, J.-P.; Nečada, M.; Moilanen, A.; Törmä, P. Lasing in Dark and Bright Modes of a Finite-Sized Plasmonic Lattice. *Nat. Commun.* **2017**, *8*, 13687.
- (23) Rodriguez, S. R. K.; Abass, A.; Maes, B.; Janssen, O. T.; Vecchi, G.; Rivas, J. G. Coupling Bright and Dark Plasmonic Lattice Resonances. *Phys. Rev. X* **2011**, *1*, 021019.
- (24) Wang, D.; Yang, A.; Wang, W.; Hua, Y.; Schaller, R. D.; Schatz, G. C.; Odom, T. W. Band-Edge Engineering for Controlled Multi-Modal Nanolasing in Plasmonic Superlattices. *Nat. Nanotechnol.* **2017**, *12*, 889894.
- (25) Guo, R.; Nečada, M.; Hakala, T. K.; Väkeväinen, A. I.; Törmä, P. Lasing at K Points of a Honeycomb Plasmonic Lattice. *Phys. Rev. Lett.* **2019**, *122*, 013901.
- (26) Li, R.; Bourgeois, M. R.; Cherqui, C.; Guan, J.; Wang, D.; Hu, J.; Schaller, R. D.; Schatz, G. C.; Odom, T. W. Hierarchical Hybridization in Plasmonic Honeycomb Lattices. *Nano Lett.* 2019, 19, 6435–6441.
- (27) Rodriguez, S.; Feist, J.; Verschuuren, M.; Garcia-Vidal, F.; Rivas, J. G. Thermalization and Cooling of Plasmon-Exciton Polaritons: Towards Quantum Condensation. *Phys. Rev. Lett.* **2013**, *111*, 166802.
- (28) Ramezani, M.; Halpin, A.; Fernández-Domínguez, A. I.; Feist, J.; Rodriguez, S. R.-K.; Garcia-Vidal, F.; Rivas, J. G. Plasmon-Exciton-Polariton Lasing. *Optica* **2017**, *4*, 31–37.

- (29) De Giorgi, M.; Ramezani, M.; Todisco, F.; Halpin, A.; Caputo, D.; Fieramosca, A.; Rivas, J. G.; Sanvitto, D. Interaction and Coherence of a Plasmon–Exciton Polariton Condensate. *ACS Photonics* **2018**, *5*, 3666–3672.
- (30) Lim, S. J.; Zahid, M. U.; Le, P.; Ma, L.; Entenberg, D.; Harney, A. S.; Condeelis, J.; Smith, A. M. Brightness-Equalized Quantum Dots. *Nat. Commun.* **2015**, *6*, 8210.
- (31) Livache, C.; Martinez, B.; Goubet, N.; Gréboval, C.; Qu, J.; Chu, A.; Royer, S.; Ithurria, S.; Silly, M. G.; Dubertret, B.; Lhuillier, E. A Colloidal Quantum Dot Infrared Photodetector and Its Use for Intraband Detection. *Nat. Commun.* **2019**, *10*, 2125.
- (32) Pradhan, S.; Di Stasio, F.; Bi, Y.; Gupta, S.; Christodoulou, S.; Stavrinadis, A.; Konstantatos, G. High-Efficiency Colloidal Quantum Dot Infrared Light-Emitting Diodes *via* Engineering at the Supra-Nanocrystalline Level. *Nat. Nanotechnol.* **2019**, *14*, 72.
- (33) Ladd, T. D.; Jelezko, F.; Laflamme, R.; Nakamura, Y.; Monroe, C.; OBrien, J. L. Quantum Computers. *Nature* **2010**, *464*, 45–53.
- (34) Yang, Z.; Pelton, M.; Fedin, I.; Talapin, D. V.; Waks, E. A Room Temperature Continuous-Wave Nanolaser Using Colloidal Quantum Wells. *Nat. Commun.* **2017**, *8*, 143.
- (35) Dang, C.; Lee, J.; Breen, C.; Steckel, J. S.; Coe-Sullivan, S.; Nurmikko, A. Red, Green and Blue Lasing Enabled by Single-Exciton Gain in Colloidal Quantum Dot Films. *Nat. Nanotechnol.* **2012**, *7*, 335.
- (36) Tang, J.; Kemp, K. W.; Hoogland, S.; Jeong, K. S.; Liu, H.; Levina, L.; Furukawa, M.; Wang, X.; Debnath, R.; Cha, D.; Chou, K. W.; Fischer, A.; Amassian, A.; Asbury, J. B.; Sargent, E. H. Colloidal-Quantum-Dot Photovoltaics Using Atomic-Ligand Passivation. *Nat. Mater.* 2011, 10, 765.
- (37) Kramer, I. J.; Sargent, E. H. Colloidal Quantum Dot Photovoltaics: A Path Forward. *ACS Nano* **2011**, *5*, 8506–8514.

- (38) Sukhovatkin, V.; Hinds, S.; Brzozowski, L.; Sargent, E. H. Colloidal Quantum-Dot Photodetectors Exploiting Multiexciton Generation. *Science* **2009**, *324*, 1542–1544.
- (39) Rodriguez, S.; Rivas, J. G. Surface Lattice Resonances Strongly Coupled to Rhodamine 6G Excitons: Tuning the Plasmon-Exciton-Polariton Mass and Composition. *Opt. Express* **2013**, 21, 27411–27421.
- (40) Väkeväinen, A.; Moerland, R.; Rekola, H.; Eskelinen, A.-P.; Martikainen, J.-P.; Kim, D.-H.; Törmä, P. Plasmonic Surface Lattice Resonances at the Strong Coupling Regime. *Nano Lett.* **2013**, *14*, 1721–1727.
- (41) Shi, L.; Hakala, T.; Rekola, H.; Martikainen, J.-P.; Moerland, R.; Törmä, P. Spatial Coherence Properties of Organic Molecules Coupled to Plasmonic Surface Lattice Resonances in the Weak and Strong Coupling Regimes. *Phys. Rev. Lett.* **2014**, *112*, 153002.
- (42) Zakharko, Y.; Rother, M.; Graf, A.; Hahnlein, B.; Brohmann, M.; Pezoldt, J.; Zaumseil, J. Radiative Pumping and Propagation of Plexcitons in Diffractive Plasmonic Crystals. *Nano Lett.* 2018, 18, 4927–4933.
- (43) Lee, B.; Liu, W.; Naylor, C. H.; Park, J.; Malek, S. C.; Berger, J. S.; Johnson, A. C.; Agarwal, R. Electrical Tuning of Exciton–Plasmon Polariton Coupling in Monolayer MoS₂ Integrated with Plasmonic Nanoantenna Lattice. *Nano Lett.* **2017**, *17*, 4541–4547.
- (44) Guo, R.; Derom, S.; Väkeväinen, A.; van Dijk-Moes, R.; Liljeroth, P.; Vanmaekelbergh, D.; Törmä, P. Controlling Quantum Dot Emission by Plasmonic Nanoarrays. *Opt. Express* **2015**, 23, 28206–28215.
- (45) Laux, F.; Bonod, N.; Gerard, D. Single Emitter Fluorescence Enhancement with Surface Lattice Resonances. *J. Phys. Chem. C* **2017**, *121*, 13280–13289.
- (46) Hamans, R. F.; Parente, M.; Castellanos, G. W.; Ramezani, M.; Rivas, J. G.; Baldi, A. Super-

- Resolution Mapping of Enhanced Emission by Collective Plasmonic resonances. *ACS Nano* **2019**, *13*, 4514–4521.
- (47) Vasa, P.; Lienau, C. Strong Light–Matter Interaction in Quantum Emitter/Metal Hybrid Nanostructures. *ACS Photonics* **2017**, *5*, 2–23.
- (48) Vasa, P.; Wang, W.; Pomraenke, R.; Lammers, M.; Maiuri, M.; Manzoni, C.; Cerullo, G.; Lienau, C. Real-Time Observation of Ultrafast Rabi Oscillations Between Excitons and Plasmons in Metal Nanostructures with J-Aggregates. *Nat. Photonics* 2013, 7, 128–132.
- (49) Garraway, B. M. The Dicke Model in Quantum Optics: Dicke Model Revisited. *Phil. Trans. R. Soc. A.* **2011**, *369*, 1137–1155.
- (50) Shahbazyan, T. V. Exciton–Plasmon Energy Exchange Drives the Transition to a Strong Coupling Regime. *Nano Lett.* **2019**, *19*, 3273–3279.
- (51) Bohren, C. F.; Huffman, D. R. *Absorption and Scattering of Light by Small Particles*; John Wiley & Sons: New York, 1998; pp 99–103.
- (52) Antosiewicz, T. J.; Apell, S. P.; Shegai, T. Plasmon–Exciton Interactions in a Core–Shell Geometry: from Enhanced Absorption to Strong Coupling. *ACS Photonics* **2014**, *1*, 454–463.
- (53) Zengin, G.; Gschneidtner, T.; Verre, R.; Shao, L.; Antosiewicz, T. J.; Moth-Poulsen, K.; Kall, M.; Shegai, T. Evaluating Conditions for Strong Coupling Between Nanoparticle Plasmons and Organic Dyes Using Scattering and Absorption Spectroscopy. *J. Phys. Chem. C* 2016, 120, 20588–20596.
- (54) Delga, A.; Feist, J.; Bravo-Abad, J.; Garcia-Vidal, F. Theory of Strong Coupling Between Quantum Emitters and Localized Surface Plasmons. *J. Opt.* **2014**, *16*, 114018.
- (55) Liu, W.; Wang, Y.; Zheng, B.; Hwang, M.; Ji, Z.; Liu, G.; Li, Z.; Sorger, V. J.; Pan, A.; Agarwal, R. Observation and Active Control of a Collective Polariton Mode and Polaritonic

- Band Gap in Few-Layer WS₂ Strongly Coupled with Plasmonic Lattices. *Nano Lett.* **2020**, 20, 790–798.
- (56) Henzie, J.; Barton, J. E.; Stender, C. L.; Odom, T. W. Large-Area Nanoscale Patterning: Chemistry Meets Fabrication. *Acc. Chem. Res.* **2006**, *39*, 249–257.
- (57) Indukuri, C.; Yadav, R. K.; Basu, J. K. Broadband Room Temperature Strong Coupling Between Quantum Dots and Metamaterials. *Nanoscale* **2017**, *9*, 11418–11423.
- (58) Linton, C. M. Lattice Sums for the Helmholtz Equation. SIAM Rev. 2010, 52, 630–674.
- (59) Campione, S.; Capolino, F. Ewald Method for 3D Periodic Dyadic Green's Functions and Complex Modes in Composite Materials Made of Spherical Particles Under the Dual Dipole Approximation. *Radio Sci.* **2012**, *47*, 1–11.
- (60) Reid, H. SCUFF-EM. 2019; http://github.com/homerreid/scuff-EM.
- (61) Grahn, P.; Shevchenko, A.; Kaivola, M. Electromagnetic Multipole Theory for Optical Nanomaterials. *New J. Phys.* **2012**, *14*, 093033.
- (62) Calculating Absorbed Optical Power Higher Accuracy. https://support.lumerical.com/hc/en-us/articles/360034915693, (accessed May 5, 2020).